The Astrophysical Journal, 731:7 (11pp), 2011 April 10 doi:10.1088/0004-637X/731/1/7

USING FARADAY ROTATION TO PROBE MAGNETOHYDRODYNAMIC INSTABILITIES IN INTRACLUSTER MEDIA

Tamara Bogdanović[1,3], Christopher S. Reynolds[1], and Richard Massey[2]
[1] Department of Astronomy, University of Maryland, College Park, MD 20742-2421, USA; tamarab@astro.umd.edu
[2] Royal Observatory Edinburgh, Blackford Hill, Edinburgh EH9 3HJ, UK
Received 2010 May 12; accepted 2011 February 8; published 2011 March 16

ABSTRACT

It has recently been suggested that conduction-driven magnetohydrodynamic (MHD) instabilities may operate at all radii within an intracluster medium (ICM) and profoundly affect the structure of a cluster's magnetic field. Where MHD instabilities dominate the dynamics of an ICM, they will re-orient magnetic field lines *perpendicular* to the temperature gradient inside a cooling core or *parallel* to the temperature gradient outside it. This characteristic structure of magnetic field could be probed by measurements of polarized radio emission from background sources. Motivated by this possibility we have constructed three-dimensional models of a magnetized cooling-core cluster and calculated Faraday rotation measure (RM) maps in the plane of the sky under realistic observing conditions. We compare a scenario in which magnetic field geometry is characterized by conduction-driven MHD instabilities to that where it is determined by isotropic turbulent motions. We find that future high-sensitivity spectropolarimetric measurements of RM, such as will be enabled by the Expanded Very Large Array and Square Kilometer Array, can distinguish between these two cases with plausible exposure times. Such observations will test the existence of conduction-driven MHD instabilities in dynamically relaxed cooling-core clusters. More generally, our findings imply that observations of Faraday RM should be able to discern physical mechanisms that result in qualitatively different magnetic field topologies, without a priori knowledge about the nature of the processes.

Key words: galaxies: clusters: general – instabilities – magnetic fields – magnetohydrodynamics (MHD) – plasmas – polarization

Online-only material: color figures

1. INTRODUCTION

Understanding the role and evolution of magnetic fields in clusters of galaxies is of significant importance for many questions including the origin of cluster magnetic fields, the interaction of active galactic nuclei (AGNs) with the intracluster medium (ICM), and physical processes operating within the ICM plasma.

One of the key techniques used to obtain information about the strength and structure of cluster magnetic fields is the analysis of Faraday rotation from polarized radio sources located behind and within clusters. The Faraday effect rotates the polarization plane of electromagnetic waves traveling through a magnetized plasma, by an amount proportional to the (square of the) wavelength, plasma density, and the strength of the field in the direction of propagation. The sources' intrinsic polarization need not be known, as the effect can be observed as a characteristic wavelength-dependent rotation measure (RM) signature. Observations of a few nearby clusters have established the presence of magnetic fields with typical strengths of few μG in non-cool core clusters and in excess of 10 μG in the centers of cool core clusters (Carilli & Taylor 2002; Govoni & Feretti 2004; Feretti & Giovannini 2008). Detailed high-resolution RM images of radio galaxies in merging and cooling-core clusters indicate that the RM distribution is characterized by patchy structures of a few kpc in size. Furthermore, the RM distribution appears in general in good agreement with the RM expected for magnetic fields geometry characterized by turbulent motions with a power-law power spectrum (for e.g., Enßlin & Vogt 2003; Murgia et al. 2004; Guidetti et al. 2008; Laing et al. 2008; Bonafede et al. 2010). This base of knowledge will be greatly enhanced by radio observatories such as the Expanded Very Large Array[4] (EVLA) and Square Kilometer Array[5] (SKA), which will provide the sensitivity to study both background and embedded sources with sufficient density to map out the RM patterns in many and more distant clusters. This will allow the structure of magnetic field to be studied in "quiescent" regions of clusters, away from radio galaxies, as well as the effect of the radio-mode feedback in their vicinity.

The interpretation of these results can strongly benefit from advances in the theoretical understanding of the dynamics of weakly magnetized, low density plasmas. The ICM is a dilute plasma, i.e., the gyrofrequency of both the electrons and the ions is much greater than the collision frequency. The principal effect of this is highly anisotropic thermal conduction that fundamentally alters the classical Schwarzschild criterion for convection (Balbus 2000). Under these circumstances, the outer regions of clusters where temperature decreases with radius may become susceptible to a conduction-driven *magneto-thermal instability* (MTI). The properties of this instability have been studied in magnetohydrodynamic (MHD) simulations (Parrish & Stone 2005, 2007; Parrish et al. 2008). Parrish et al. (2008) found that MTI can profoundly affect the temperature distribution in the outer regions of a cluster in only a few billion years, by re-orienting the lines of magnetic field to be preferentially radial, resulting in a thermal conduction at a high fraction of the Spitzer conductivity.

The temperature profile in the centers of cooling-core galaxy clusters makes them stable to MTI. However, Quataert (2008)

[3] Einstein Postdoctoral Fellow.

[4] http://science.nrao.edu/evla
[5] http://www.skatelescope.org

found that cooling cores are characterized by a sister *heat-flux buoyancy instability* (HBI) that arises in regions where temperature increases with radius. An initial investigation of nonlinear evolution of the HBI (Parrish & Quataert 2008) indicates that its primary effect is to re-orient the lines of magnetic field perpendicular to the temperature gradient, and thus strongly suppress heat conduction. The properties of HBI have been investigated in global three-dimensional (3D) models of isolated cooling-core clusters (Parrish et al. 2009; Bogdanović et al. 2009). They suggest that, once the magnetic field lines have been wrapped into spherical surfaces surrounding the core, the effective thermal conduction is suppressed to a small fraction of the Spitzer value, leading to insulation of the core from further conductive heating, and to a subsequent thermal collapse.

Very recently, Balbus & Reynolds (2010) discovered an associated pair of *overstabilities* that affect precisely those configurations that are stable to the well-established HBI and MTI. They predict that configurations which tend to result from the nonlinear evolution of the HBI have g-modes that are driven overstable by radiative loses. On the other hand, configurations which tend to result from the nonlinear evolution of the MTI have g-modes that are driven overstable by the conductive heat flux. The effects of these overstabilities for the ICM plasma thermodynamics and the properties of magnetic field are yet to be understood. We do not consider them in this work and instead focus on MTI and HBI instabilities.

The combination of MTI and HBI instabilities should lead to a characteristic structure of magnetic fields in some cooling-core clusters. If these conduction-driven instabilities dominate the dynamics of the ICM, the magnetic field lines would be preferentially oriented radially in the outer region and azimuthally within the cooling core. This may not be the case in all clusters—it has recently been shown that MHD instabilities can be overwhelmed by even moderate levels of driven turbulence (Ruszkowski & Oh 2010; Parrish et al. 2010), such as might result from sub-cluster mergers, motions of cluster member galaxies, or various forms of AGN feedback. Which (if any) physical mechanism dominates in the ICM depends sensitively upon the magnitude and distribution of turbulence, which is currently only poorly understood. Motivated by this question and guided by the MHD simulations, we have constructed 3D models of clusters for two distinct cases and simulated the RM maps that might be observed with high-sensitivity radio polarization measurements.

This paper is organized as follows. We describe the ingredients of our cluster models in Section 2 and the main properties of derived RM maps in Section 3. We discuss the importance of depolarization and diffuse emission in Section 4, then present the discussion with conclusions in Section 5.

2. CLUSTER MODELS

2.1. Intracluster Medium and Magnetic Fields

Any magnetized cluster acts as a Faraday screen for polarized sources located behind a cluster or in the cluster itself. Modeling the RM signature of such a cluster will require several main ingredients: the density and temperature distribution of electrons in the ICM of the cluster, the 3D structure of the magnetic field, and the density and fluxes of polarized background sources. We construct models in a Cartesian coordinate system (x, y, z) with a cubic spatial domain defined by $x = \pm L$, $y = \pm L$, $z = \pm L$, where $L = 300$ kpc. For the electron density and temperature distributions, we adopt analytic approximations based on the *XMM-Newton* observations of the Perseus cluster that capture the radial behavior of these two parameters (we use expressions from Churazov et al. 2003 and scale them to our assumed cosmology):

$$n_e = \frac{3.9\times10^{-2}}{[1+(r/r_a)^2]^{1.8}} + \frac{4.05\times10^{-3}}{[1+(r/r_b)^2]^{0.87}}\ \mathrm{cm}^{-3}\ , \quad (1)$$

$$T_e = 7\frac{[1+(r/r_c)^3]}{[2.3+(r/r_c)^3]}\ \mathrm{keV}\ , \quad (2)$$

where $r = (x^2+y^2+z^2)^{1/2}$ is in units of kiloparsecs and $r_a = 56.5$ kpc, $r_b = 197.7$ kpc, and $r_c = 70.6$ kpc. The central electron number density and temperature are $n_e(0) = 4.3\times10^{-2}\,\mathrm{cm}^{-3}$ and $T_e(0) = 3\,\mathrm{keV}$, respectively.

We consider two models of the cluster's magnetic field. Our first model (model A) is motivated by the results of recent MHD simulations of instabilities in the ICM, where the magnetic field is preferentially azimuthal within the cooling core and radial outside of this region. Hence, in a spherical polar coordinate system (r, θ, ϕ), where $\theta = 0$ is aligned along the z-axis, the field structure within the cooling core, $r \leqslant r_c = 200$ kpc, is described in terms of only θ and ϕ components (Bogdanović et al. 2009):

$$B_\theta = 2B_0(1+\sin(2\pi r/r_1))\sin\theta\cos(2\phi), \quad (3)$$

$$B_\phi = 2B_0(1+\sin(2\pi r/r_2))\sin(3\theta) - B_0(1+\sin(2\pi r/r_1))\sin(2\phi)\sin(2\theta). \quad (4)$$

$B_0(r)$ is chosen so that the value of the plasma parameter, $\beta = 8\pi n_e\, k\, T_e/B_0^2 = 100$, is constant everywhere within the cooling-core region. This implies $B_0(0) = 7.3\,\mu$G at the cluster center, the field strength in the range 2.3×10^{-5}–$36.2\,\mu$G, and mean strength over the computational volume of $3.3\,\mu$G. $r_1 = 7.5$ kpc and $r_2 = 24$ kpc are the coherence lengths defining characteristic radial scales on which the magnetic field vector changes direction. The magnetic field thus changes direction 8–26 times across the cool core radius. In addition to these two scales, Equations (3) and (4) also capture the field geometry expected to arise as a consequence of the HBI: field lines wrapped onto the spherical surfaces within the cool core. This implies that in model A magnetic field reversal also occurs on a range of spatial scales associated with the spheres of different radii and up to the size of the cool core, $2r_c = 400$ kpc. It follows that 400 kpc is the maximum scale for magnetic field fluctuations in model A.

The magnetic field structure outside of the cooling core, $r > r_c$, is described by a radial component,

$$B_r = \frac{B_{r0}}{r^2}, \quad (5)$$

where B_{r0} is defined from the condition $B_r^2(r_c) = \langle B_\theta^2(r_c) + B_\phi^2(r_c)\rangle$. The simple analytic form for the field structure given by Equations (3)–(5) satisfies the condition $\mathrm{div}\,\mathbf{B} = 0$ everywhere except at $r = r_c$, where the field lines are transitioning from azimuthal to radial. In a realistic case, this transition would be more gradual and also divergence free. We nevertheless expect that, except around $r \approx r_c$, our model should capture the salient properties of the magnetic field of a cluster affected by MHD instabilities across a wide range of radii.

Table 1
Summary of Model Properties

Model	Observatory	Scenario	N_s	d_s (kpc)	$\frac{\sum \lvert a_{n,0}\rvert}{\sum \lvert a_{n,m}\rvert}$	$\frac{\sum \lvert a_{n,1}\rvert}{\sum \lvert a_{n,m}\rvert}$	$\frac{\sum \lvert a_{n,2}\rvert}{\sum \lvert a_{n,m}\rvert}$	$\frac{\sum \lvert a_{n,3}\rvert}{\sum \lvert a_{n,m}\rvert}$
	SKA	1h, low	449	28	8.1%	39.1%	15.3%	2.1%
	SKA	1h, high	7117	7	17.3%	45.1%	15.4%	1.9%
A	SKA	100h, low	2250	13	7.8%	43.5%	17.6%	2.5%
	SKA	100h, high	89592	2	14.3%	50.0%	17.7%	0.7%
	EVLA	9h, low	65	75	11.1%	28.2%	10.5%	3.9%
	EVLA	9h, high	337	33	9.0%	39.5%	15.8%	2.4%
	SKA	1h, low	449	28	25.3%	15.6%	11.6%	5.4%
	SKA	1h, high	7117	7	11.9%	12.1%	9.4%	5.6%
B	SKA	100h, low	2250	13	19.3%	16.0%	10.4%	5.7%
	SKA	100h, high	89592	2	9.2%	7.5%	9.1%	5.7%
	EVLA	9h, low	65	75	31.1%	16.6%	13.2%	4.4%
	EVLA	9h, high	337	33	20.5%	19.6%	11.0%	7.6%

Notes. Model: A (B) corresponds to the instability-dominated (turbulence-dominated) cluster model; Observatory: one of the two radio observatories considered in the paper; Scenario: see the text; N_s: number of background polarized sources within 600 kpc × 600 kpc area; d_s: mean separation of polarized background sources; ratios: fraction of the total RM intensity in circularly symmetric shapelet multipoles.

In our second model (model B), magnetic field lines are randomly tangled, reflecting a different physical scenario in which the field geometry is set by the action of isotropic turbulence. While this theoretical hypothesis is most likely idealized, it is physically motivated and well rooted in theoretical practice, so we use it as a control case to model A. Following Roettiger et al. (1999), we initialize the field geometry by defining a magnetic field potential in Fourier space of $\tilde{A}(k) = \tilde{A}_0 k^{-\alpha}$, where each Cartesian factor $\tilde{A}_0$ has an amplitude drawn from a Gaussian distribution and a random phase, assuring uncorrelated modes. We convert this into real space via a 3D fast Fourier transform (FFT). The tangled magnetic field is then calculated as $\mathbf{B} = \nabla \times \mathbf{A}$. We adopted $\alpha = 17/6$, which results in the Kolmogorov-like power spectrum $B^2 \propto k^{2(1-\alpha)} \propto k^{-11/3}$. The smallest and largest magnetic structures produced by this power spectrum have the scales of $\lambda_{\rm min} = 2\pi/k_{\rm max} = 7.5$ kpc and $\lambda_{\rm max} = 2\pi/k_{\rm min} = 600$ kpc, respectively. The magnitude of magnetic field is normalized in such way that the azimuthally averaged magnetic energy comprises 1% of the thermal energy of the gas at all radii (i.e., $\beta = 100$, same as in model A). This implies the mean magnetic field strength decreasing with the distance from the cluster center and $B_0(0) = 7.3\,\mu$G. The field strength in model B varies between 8.3×10^{-8} and 29.8 μG, and its mean amplitude over the computational volume is 1.3 μG.

2.2. Observational Scenarios

We place the model cluster at the redshift of the Perseus cluster, which is a suitable prototype for a nearby cooling-core cluster. At the distance of NGC 1275 ($z = 0.0176$; Strauss et al. 1992), the central bright galaxy in Perseus, $1''$ corresponds to 353 pc.[6] To simulate future, high-sensitivity RM surveys, we adopt the planned capabilities of the soon to be fully operational EVLA and the next-generation radio interferometer, SKA, at 1.4 GHz.

EVLA consists of twenty-seven 25 m diameter antennas that will provide an order-of-magnitude increase in sensitivity above the existing Very Large Array after it is upgraded with new receivers and electronics. Together with improved resolution and imaging, these new capabilities make EVLA an important tool for studies of Faraday rotation in the near future.[7] Its technical specifications include a continuous coverage with full polarization capabilities between frequencies of 1 and 50 GHz, a field of view (FOV) of ∼0.25 deg^2 at 1.4 GHz, and angular resolution as high as $\theta_{\rm EVLA} = 1''.3$ (achievable in the largest array configuration; A-configuration) also at 1.4 GHz ($\lambda = 21$ cm). Furthermore, observations of the continuum emission with the EVLA are expected to achieve the rms noise limit of 1.6 μJy/beam between 1 and 2 GHz in about 9 hr of exposure. In the next step we will use this sensitivity limit to estimate the density of the background polarized sources on the sky that will be seen by the EVLA at 1.4 GHz.[8]

With further improvements in sensitivity and survey speed over current instruments, SKA will be ideally equipped to study the origin and evolution of cosmic magnetism in the future (Carilli & Rawlings 2004; Dewdney et al. 2009; Krause et al. 2009).[9] Planned technical specifications for the SKA include a square kilometer collecting area, continuous frequency coverage from 70 MHz to 25 GHz, a FOV of 1 deg^2 at 1.4 GHz, and angular resolution better than $\theta_{\rm SKA} = 1''$ at the same frequency (Schilizzi et al. 2007; Taylor 2008). Note however that the frequency range for RM studies with the SKA will be relatively wide (∼0.3–10 GHz) and that the exact FOV and angular resolution depend on the frequency. Observations with the SKA are expected to achieve an rms noise of 0.1 μJy/beam area and 0.01 μJy/beam area at 1.4 GHz within 1 hr and 100 hr of integration, respectively (Carilli & Rawlings 2004).

Given the EVLA and SKA sensitivity limits, we follow approach in Stepanov et al. (2008) to estimate the number density of polarized background sources at 1.4 GHz expected for our model cluster. Stepanov et al. (2008) extrapolate the source counts at 1.4 GHz from $P = 0.5$ mJy to the limiting flux density of $P_{\rm min} = 0.05\,\mu$Jy using a power-law relation between the cumulative number of sources per square degree and polarized flux density, $N_\square(>P) \propto P^{-\gamma}$. The exponent γ can take a range of values between 0.7 and 1.1, which correspond to the low and high bounds for the source counts at a given flux

[6] Throughout this paper, we adopted a ΛCDM cosmology with $H_0 = 71\,{\rm km\,s^{-1}\,Mpc^{-1}}$, $\Omega_m = 0.27$, and $\Omega_\Lambda = 0.73$.

[7] Currently, EVLA is on schedule for completion at the end of 2012.

[8] Information about the EVLA capabilities and specifications was obtained from http://www.vla.nrao.edu/astro/guides/vlas/current/.

[9] At this point a commencement of full science operations with the SKA is planned for 2020.

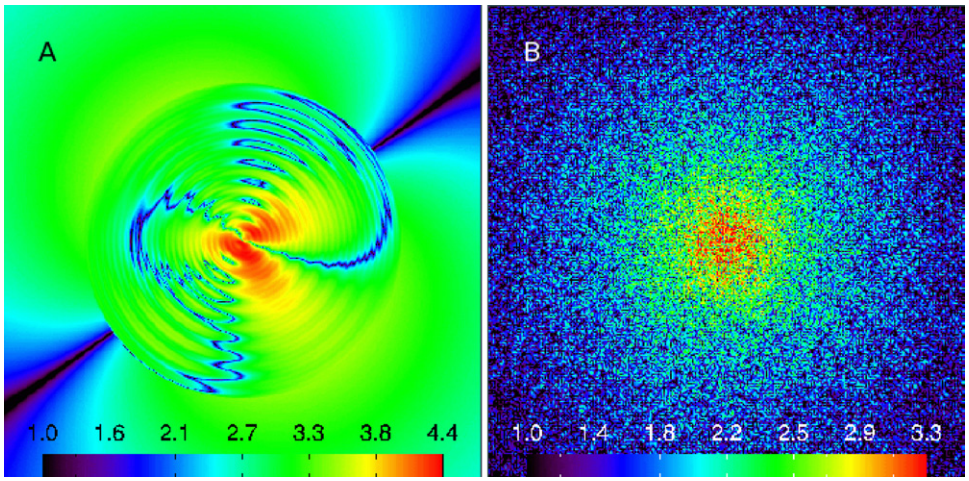

Figure 1. Simulated continuous Faraday rotation measure maps for an instability-dominated (model A) and turbulence-dominated (model B) cluster. Panel size is 600 kpc on a side and the color scale shows log |RM|. In model A, two distinct regions are visible: the magnetic field is dominated by HBI inside the cooling core, and MTI outside. The diagonal feature at large radii is an artifact of the model. In model B, the cluster's magnetic field is randomly tangled, producing a patchy RM distribution.

(A color version of this figure is available in the online journal.)

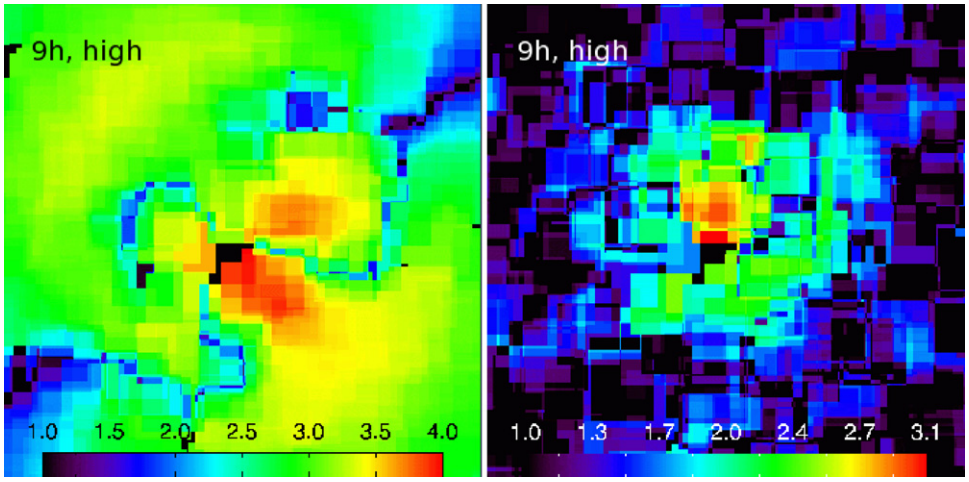

Figure 2. Faraday rotation measure maps simulated for a 9 hr exposure with EVLA in a high source count observational scenario. Panels show instability-dominated cluster considered in model A (left) and turbulence-dominated cluster from model B (right). Panels show the same region and color scaling as in Figure 1.

(A color version of this figure is available in the online journal.)

limit at 1.4 GHz. We consider exposure times of 9 hr in case of EVLA and 1 hr and 100 hr for SKA, both in the low and high source count scenarios, thus obtaining a total of six different observational scenarios for both models A and B. In Table 1 we list the total number of background polarized sources (N_s) with polarized flux densities $>5\sigma_P$ above the noise, within a 600 kpc × 600 kpc area centered on the cluster. Also shown is the mean separation between the sources (d_s) at the redshift of the cluster.

Note that in the estimation of the number of background polarized sources we simply extrapolated the number of sources from 0.5 mJy down to the μJy and nJy flux densities. The nature of the dominant population of sources that EVLA and SKA will detect at such low flux densities is uncertain, as they lie beneath the surface of the deepest radio surveys that are currently available. It has been proposed that the μJy and nJy sky is dominated by radio-quiet AGNs and star-forming galaxies (Jarvis & Rawlings 2004; Wilman et al. 2008) as well as faint ellipticals and dwarf galaxies (Padovani 2010). It is also worth pointing out a simplification in our modeling which stems from an assumption that all background polarized sources are point like, while in reality some low redshift background sources will have a resolved extended structure. We nevertheless expect these to comprise a small fraction, as a majority of sources are expected to reside at high redshifts.

3. FARADAY ROTATION MEASURE MAPS

3.1. Construction and Properties

The polarization of electromagnetic waves traveling through the cluster's magnetic field is rotated by an angle $\Delta\chi = \mathrm{RM}\,\lambda^2/(1+z)^2$, where λ is the observing wavelength and z is the redshift of the Faraday screen. We calculate the effect of this Faraday rotation for our model cluster by numerically integrating the expression $\mathrm{RM} = 812\,\mathrm{rad\,m^{-2}} \int n_e\,\mathbf{B}\cdot\mathbf{dl}$, where n_e is the electron number density in units of cm^{-3}, $\mathbf{B}$ is the vector of magnetic field in μG, and $\mathbf{l}$ is the vector demarking the depth of the magnetic screen in kiloparsecs as measured along the line of sight of an observer placed at infinity, at an arbitrary orientation with respect to the cluster. The result is a two-dimensional (2D), continuous map of RM intensity with $\sim 1''$ resolution shown in Figure 1. We convolve this map with

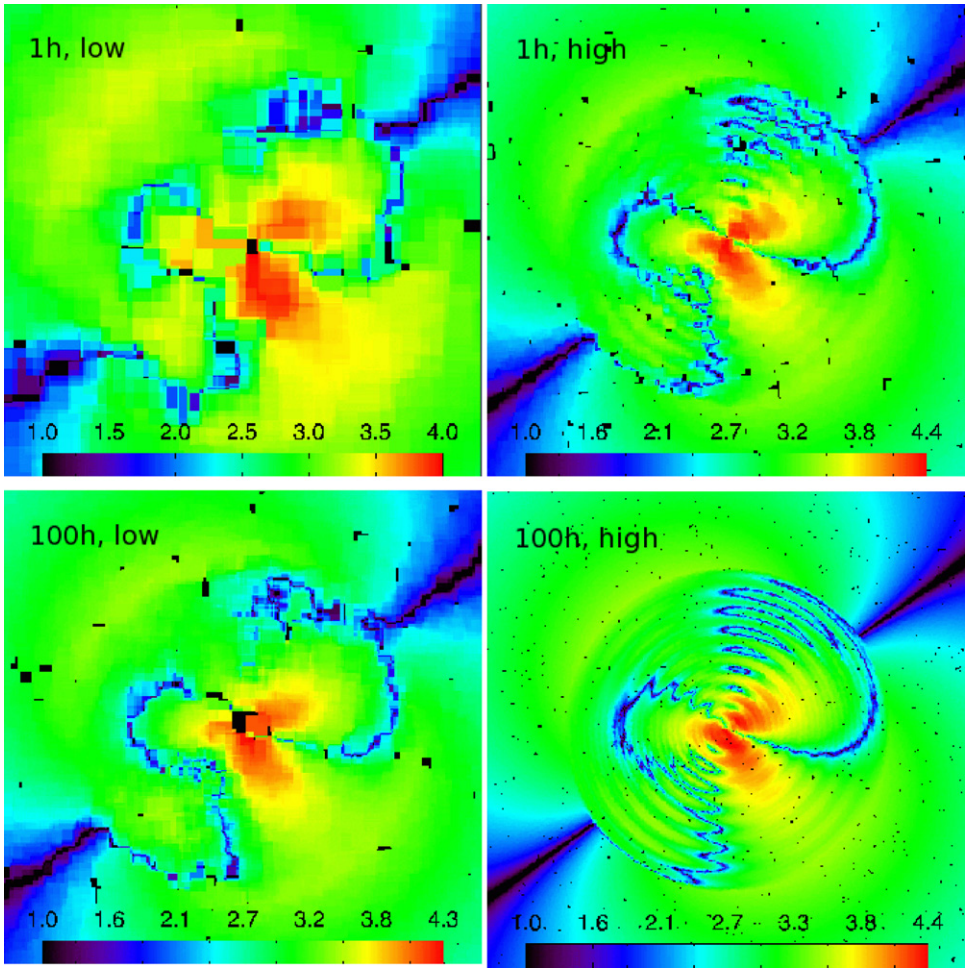

Figure 3. Simulated SKA Faraday rotation measure maps for an instability-dominated (model A) cluster. The four observing scenarios include short or long exposure times, with low or high background source densities. Panel size and color scale are the same as in previous figures.

(A color version of this figure is available in the online journal.)

a map of point like, randomly distributed polarized background sources, where the number of sources in the map is N_s. For visual representation in Figures 2, 3, and 4 the convolved maps are smoothed with a box function, where the size of each box is chosen so that it contains five polarized background sources on average. This implies a smoothing box of the size $h_{\rm box} = 69$ kpc for the EVLA "9h, high" scenario and $h_{\rm box} = 60$, 15, 26.4, and 4.2 kpc for the SKA scenarios "1h, low," "1h, high," "100h, low," and "100h, high," respectively. We list the properties of the RM maps in Table 1.

Figure 2 shows maps for the models A (left panel) and B (right panel) calculated for a 9 hr exposure with EVLA in the scenario with an assumed high count of background polarized sources. The RM structure in both appears marginally resolved. The 9h, low scenario results in unresolved RM structure (the RM map for this case is not shown but its properties are listed in Table 1, for comparison). This is not surprising given the low number density of background sources within the considered area with average spacing between the sources of $d_s \approx 75$ kpc, demarking the effective size of the "resolution element" in this scenario. Figures 3 and 4 show the RM maps for models A and B, realized in each of the four observational scenarios with the SKA. In both, the instability-dominated and turbulence-dominated scenarios, the quality and spatial sampling of the maps increase with the density of background polarized sources, to the degree that the most optimistic observational scenario with the SKA, 100h, high, almost exactly replicates the features of the continuous RM maps shown in Figure 1. This is implied by the hierarchy of characteristic scales, $\theta_{\rm SKA} < d_s < \lambda_{\rm min}$, meaning that both the angular resolution of the SKA and the density of the background polarized sources are sufficient to fully capture the spectrum of the ∼kpc scale RM variations in this model.

In all observational scenarios of model A it is possible to discern two distinct regions, which are characterized by the HBI (core) and MTI (outer region) instabilities. The dark swirl patterns in the cooling-core region, with low values of RM, arise where the magnetic field changes direction along the line of sight. Because of the multiple magnetic field reversals along the lines of sight, the RM intensity ridges in the core do not correspond to the magnetic field structure in a trivial way. Nevertheless, they carry an imprint of the azimuthal distribution of the field lines, and if indeed present in cooling-core clusters, may be one of the characteristic features to search for in RM surveys of clusters. Outside of the core, where the magnetic field geometry is radial with decreasing magnitude, the RM intensity also decreases smoothly with radius. The diagonal feature apparent in maps calculated for model A, in the left panel of Figure 2 and all panels of Figure 3, is an artifact of our model: the underlying symmetry in the radial component of the magnetic field causes a cancellation in the RM along these lines of sight resulting in low values of RM. The black specks occur in places where the number of background sources per

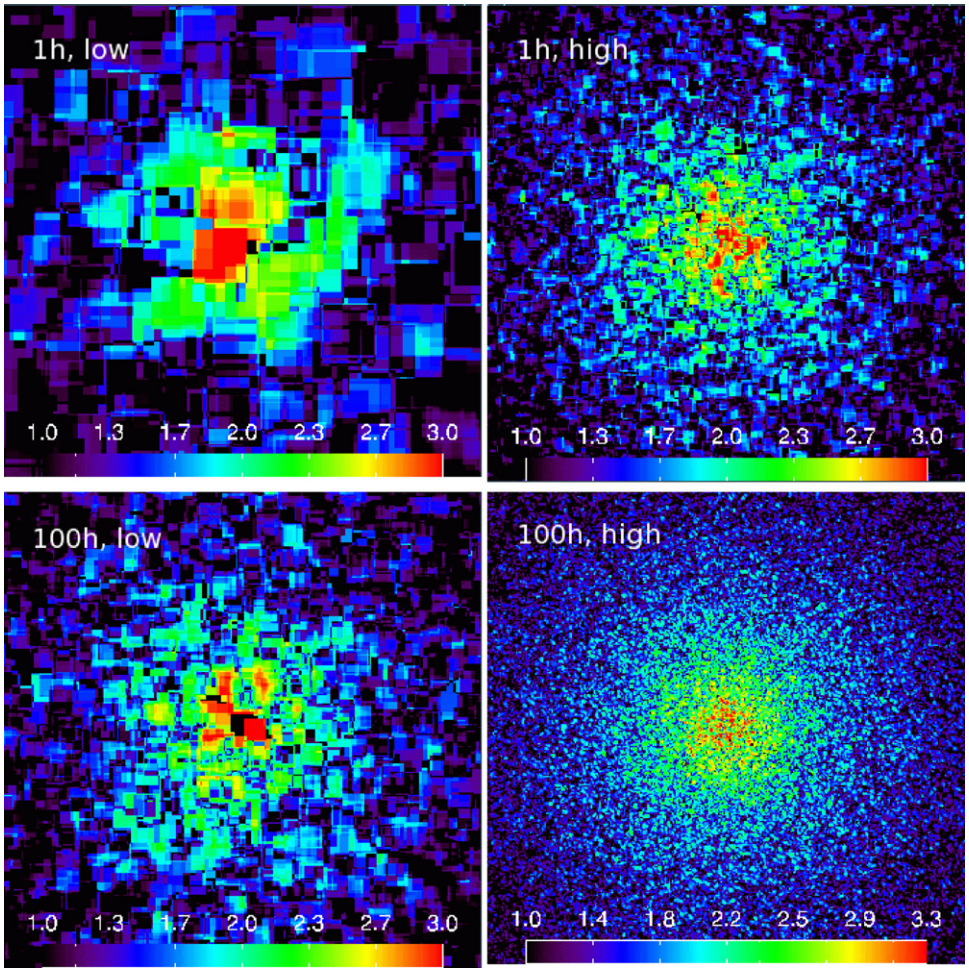

Figure 4. Simulated SKA Faraday rotation measure maps for a turbulence-dominated (model B) cluster, in four observational scenarios. Panel size and color scale are the same as in previous figures.

(A color version of this figure is available in the online journal.)

smoothing box falls to zero. The lower cutoff value applied in maps (10 rad m^{-2}) is comparable to the maximum error of RM reached at the limiting flux density $P_{\rm min} = 5\sigma_P$ with the EVLA and SKA (Stepanov et al. 2008).

In model B, shown in the right panel of Figure 2 and in Figure 4, the RM patterns exhibit a noticeably different, patchy distribution. The local maxima (minima) of the RM distribution are again associated with regions where magnetic field reversal results in an enhancement (a cancellation) along the line of sight. The main difference in model B is that the cancellation effect is more pronounced relative to model A, due to the tangled geometry of the magnetic field, even though the assumed magnetic field strength is comparable in both models (see Section 2.1). This results in the maximum RM value about an order of magnitude lower than in the model A, where the magnetic field lines exhibit uniformity and azimuthal structure on large scales.

3.2. Discrimination between Cluster Models

An image analysis technique well suited to characterizing the different geometric patterns in the RM maps is *polar shapelets* (Massey & Refregier 2005). This is based on the unique decomposition of localized objects into a series of orthogonal basis functions that explicitly separate modes with different rotational symmetries. Useful forms exist in both 2D and 3D. The former can generally be used for accurate object photometry and astrometry (Kuijken 2008), as well as morphological classification of the images of galaxies (Kelly & McKay 2005; Massey et al. 2007), magnetograms of sunspots (Young et al. 2005), and the response of the human visual cortex (Victor et al. 2009). Its convenient mathematical properties and intuitive interpretation also make it a particularly effective morphology estimator for clusters' magnetic fields.

We fit each image $I(\mathbf{x})$ in Figures 2, 3, and 4 as a weighted sum of shapelet basis functions $\chi_{n,m}(x, y)$ such that

$$I(x, y) = \sum_{n=0}^{30} \sum_{m=-n}^{n} a_{n,m}\, \chi_{n,m}(x, y), \qquad (6)$$

where the (complex) coefficients $a_{n,m}$ describe the power in modes with n radial oscillations and m-fold rotational symmetry, similar to a localized Fourier transform. Higher n-orders also capture structure at increasing distances from the cluster core. In general, the sum over n can extend to infinity, although in practice we have arbitrarily truncated it to 30. The sum over m need include only every other term, because the intervening basis functions are explicitly zero. We focus our analysis on the inner 600 kpc region of the modeled cluster, which encloses the most interesting RM patterns, and show the magnitudes of the derived shapelet coefficients $a_{n,m}$ in Figures 5, 6, and 7.

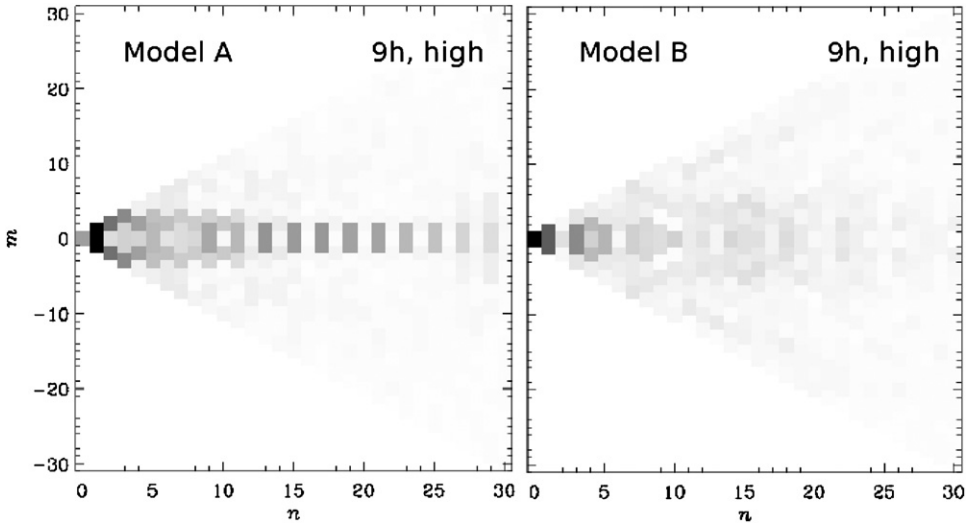

Figure 5. Polar shapelet decomposition of the RM images for model A (left) and model B (right) in observational scenario 9 h, high with EVLA. The amplitude of multipole coefficients is indicated by the linear gray scale, with darker colors corresponding to higher amplitudes. The (complex) shapelet coefficients also have phases, which indicate the orientation of each multipole, but these are not shown.

The analysis of the maps for different observational scenarios within model A (or model B) gives qualitatively similar results, but with varying ratios of signal to noise. The key idea is that the shapelet decomposition efficiently isolates modes of rotational symmetry present in the RM maps, even in the presence of significant observational noise. Indeed, the distribution of power in the two models is strikingly different. The shapelet decomposition of scenarios in model A shows almost all power within the range $m = \{-3, 3\}$, while it fans out uniformly over m in turbulent model B. The radially symmetric ($m = 0$) modes describe the average, uniform level of the RM intensity. The restriction of model A's deviations from dipole ($|m| = 1$), quadrupole ($|m| = 2$), and sextupole ($|m| = 3$) modes with low orders of rotational symmetry can be understood in light of the equivalent θ and ϕ terms in Equations (3) and (4). For each model, Table 1 lists the fraction of power in shapelet coefficients with $|m| = 0$–3, as estimators similar to the shapelet asymmetry estimator (Equation (61) of Massey et al. 2007).

In all the observational scenarios that we have considered, the magnetic field geometry of model A is distinguished from that of model B as a large fraction of RM power in modes $|m| \leqslant 3$ and a decreasing power in higher-$|m|$ modes. In scenarios with a low density of background polarized sources, namely 9h, high (left panel of Figure 5) and 1h, low (top left panel of Figure 6), the observed RM measure map has insufficient resolution to contain all the $|m| = 3$ modes, so the cutoff is present but less distinct. That the two EVLA and SKA observational scenarios are indeed similar is indicated by the comparable polarized source densities and similar distributions of the RM intensity (Table 1). Most excitingly, even in observing scenarios with noisier data, which may be achieved in longer exposures with EVLA and relatively short exposures with SKA, the large-scale magnetic field patterns are efficiently captured by polar shapelets. In the remaining observational scenarios for the SKA, characterized by the higher density of background polarized sources ("1h, high," "100h, low," and "100h, high"), the distribution of power remains very robust, as illustrated by the polar shapelet decomposition.

In model B, the power is more uniformly distributed among the azimuthal modes (m-modes), while the distribution across the radial modes (n-modes) changes with the number density of background polarized sources. In observational scenarios with the lower density of sources ("9h, high," "1h, low" and "100h, low"), a significant fraction of the power is in lower n-modes and thus the RM structure is captured on larger scales and not captured on small scales. With the increasing density of polarized sources some of the power shifts uniformly toward higher m- and n-modes (see 1h, high scenario), indicating that finer RM structures are beginning to be resolved in this scenario.

A practical implementation of the shapelet decomposition also requires advance estimates of a cluster's center and size, so that the basis functions can be constructed at a given location. For this analysis, we iteratively optimized the size of the basis functions to minimize residuals between the simulated RM map and its shapelet model. The scale factor of the basis functions represents the size of the Gaussian used in image deconstruction. In combination with the maximum (truncation) value of n in the model, it determines its resolution in such way that smaller values of the scale factor allow higher resolution models. The same scale size also sets the maximum spatial extent of the model, and there is a balance between the ability to model the large-scale features and the high frequency detail, a choice that is optimized via χ^2 minimization. The sizes of the basis functions used are thus naturally different in the various observational scenarios and between models A and B, depending on the detail of the RM patterns. This approach allows the characteristic scale of the smallest (resolved) RM patterns to be constrained using this iterative procedure; however, our results are robust to setting a fixed physical scale size to the reconstruction. Also for the purposes of this analysis, we assumed that the center of a cluster would be known a priori. It would be possible to determine the best-fit center via iteration on the RM image itself, but it will likely be known to better accuracy in practice from independent (e.g., optical or X-ray) observations. Spurious offsets in the center primarily shift power in the dipole $|m| = 1$ shapelet modes. Indeed, small-scale structure near the cluster core in this realization, amplified by the high electron density, is responsible for the large $a_{1,\pm1}$ and $a_{3,\pm3}$ coefficients, which correspond to basis functions with a small spatial extent. If the center were determined from these data alone, this structure would pull the center around, shifting some power between adjacent shapelet coefficients (Massey et al. 2007).

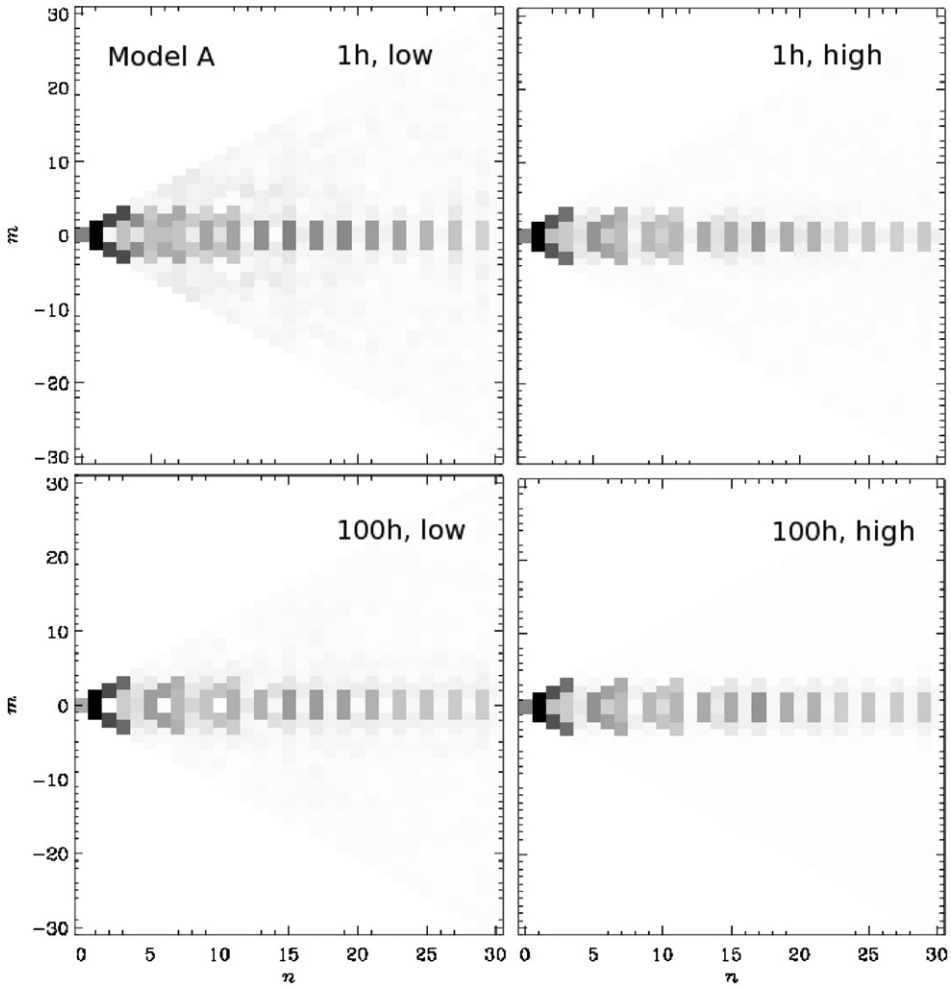

Figure 6. Polar shapelet decomposition of the RM images in model A (instability-dominated cluster) for four different observational scenarios with the SKA. Color scale is the same as in Figure 5.

We emphasize that the exact distribution of power in decomposed RM images is model dependent and that neither of our two models should be regarded as a strict prediction of future observations. More generally, our analysis demonstrates that physical mechanisms that qualitatively adjust the magnetic field distribution in clusters can easily be distinguished using observed RM maps, with plausible exposure times.

4. DEPOLARIZATION AND DIFFUSE FOREGROUND EMISSION

While the sensitivity of the instrument and (consequently) the density of observable polarized background sources strongly affect the precision of Faraday RM observations, the ability to tie the observed properties of the RM maps to the underlying magnetic field also depends on the effect of depolarization. Depolarization is a reduction of the observed degree of polarization which may arise within the cluster itself due to its spatial extent (internal depolarization) or due to limitations in instrument capabilities (beamwidth and bandwidth depolarization). We now discuss the importance of beamwidth and bandwidth depolarization in the context of our models.

Beamwidth depolarization arises when the minimum magnetic field coherence length is smaller than the beam size of the radio instrument, and cancellation of the RM occurs within the beam. Given that the assumed beamwidth in our calculation is $1'' = 353$ pc and the magnetic field coherence lengths are much larger ($\geqslant$7.5 kpc), no beamwidth depolarization is expected to occur in these scenarios. A similar effect that can lead to a small loss of information is smoothing that we apply to all of our RM images. In our simulated observations, the smoothing length varies between $\sim$4 kpc and $\sim$70 kpc, depending upon the density of background sources in a particular observational scenario, and this determines the size of the smallest RM patterns that can be inferred with confidence from a smoothed image. However, this does not represent a fundamental limitation, since more sophisticated smoothing methods and scales could be adopted on real data.

Bandwidth depolarization is the cancellation and averaging of the Faraday RM that arises in polarimeters operating in fixed, wide frequency bands. Bandwidth depolarization will be largely eliminated by the EVLA and SKA, by acquiring RM measurements via the RM synthesis method. RM synthesis is based on multichannel spectropolarimetry to enable the detection of weak, polarized emission (Brentjens & de Bruyn 2005). Most importantly, this also allows the simultaneous observation of a range of different RM values and the separation of RM components from distinct regions (such as foreground and background structures) along the line of sight. Indeed, the RM signal due to Faraday rotation of polarized light from real background sources is complicated by diffuse, intrinsic polarized emission from both the ICM plasma itself and our own Galaxy.

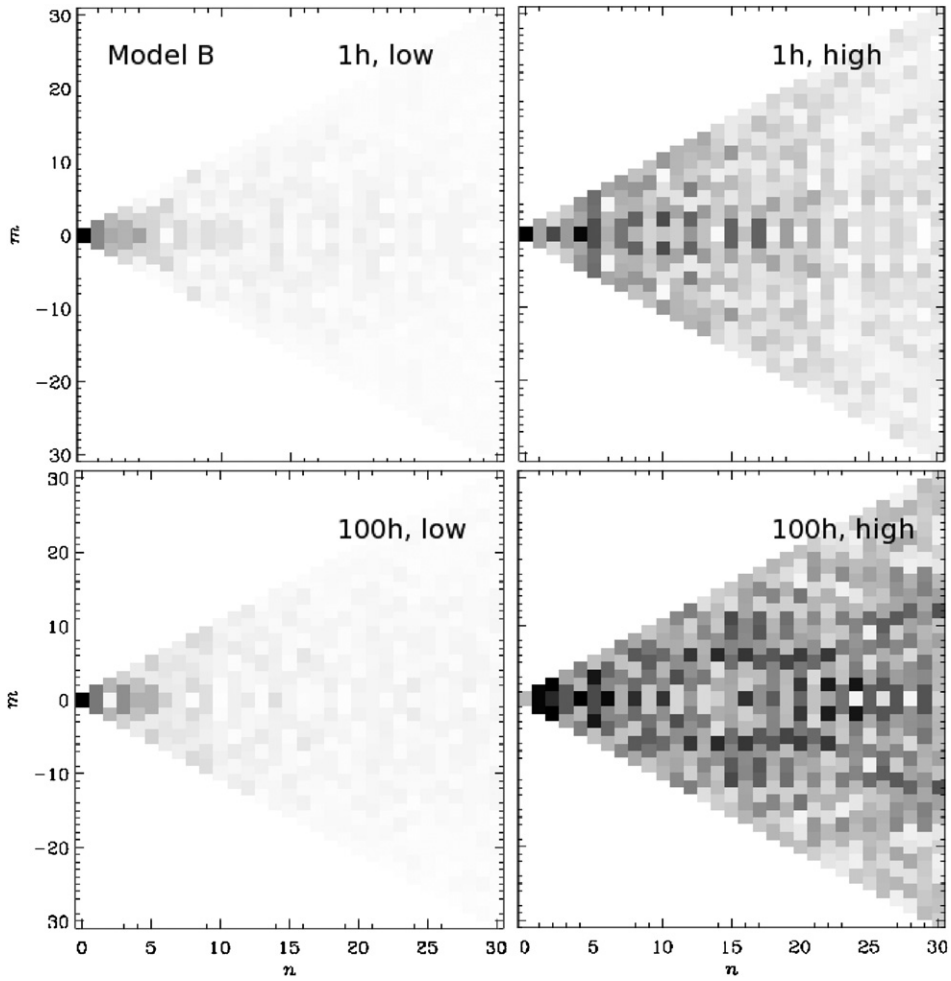

Figure 7. Polar shapelet decomposition of the RM images for model B (turbulence-dominated cluster) for four different observational scenarios with the SKA. Color scale is the same as in previous figures.

Diffuse, polarized foreground emission from cooling-core clusters can be attributed to mini-halos, steep spectrum radio sources associated with the ICM around a powerful central radio galaxy. The prototypical example is a ∼450 kpc mini-halo at the center of Perseus. Brentjens (2011) finds that the diffuse emission observed at 350 MHz in the direction of Perseus seems not to be related to the mini-halo but rather to the foreground emission from the Milky Way. Our Galaxy interferes with measurements by Faraday-rotating any extragalactic polarized signal and by adding its own polarized emission. RM of Galactic origin is typically $\sim 10\,\mathrm{rad\,m^{-2}}$ but can be as high as $300\,\mathrm{rad\,m^{-2}}$ for objects close to the Galactic plane (Simard-Normandin et al. 1981). In the direction of the Perseus cluster, for example, Brentjens (2011) measures a relatively low RM contribution (compared to our modeled values) in the range -50 to $+100\,\mathrm{rad\,m^{-2}}$, which can in principle be disentangled from the RM map of the cluster using the RM synthesis technique and is not expected to produce an RM signal competing with that from the cluster. Thus, we conclude that the RM features modeled in this work are not expected to be significantly affected by depolarization and should dominate in magnitude over any component of RM contributed by the sources of diffuse polarized emission. The primary factor that determines the efficacy of the RM maps in probing the magnetic field structure is the sensitivity of the spectropolarimetric measurements.

5. DISCUSSION AND CONCLUSIONS

Even if MTI and HBI instabilities operate uninhibited in real clusters, the radial–azimuthal field geometry is likely to be perturbed by intermittent phases of AGN activity and mergers. As these perturbations are attenuated over time, they can source a new cycle of MHD instabilities. The relics of such events, including shocks, bubbles, and ridges of magnetic field lines swept by intracluster galaxies, may also be recognizable in high-quality RM maps—testifying to the past evolution of a cluster. But with a characteristic time scale for the saturation of MHD instabilities of only a few billion years, the magnetic field lines can be driven to recover their orientation relatively quickly. As a consequence, a fraction of clusters may exhibit preferential magnetic field geometries, despite episodic disruptions.

Circumstantial evidence in support of this hypothesis may already exist in several forms. Recent detailed observations of the Virgo cluster revealed an isothermal region with remarkable azimuthal symmetry cocooned in the cool core of the cluster between the active radio lobes of M87 (Million et al. 2010). The metallicity of the isothermal gas in the same region is non-uniform and clumpy. It is reasonable to expect that the high metallicity parcels of gas were uplifted from the low entropy, cool core region of the cluster, where the density of stars is highest. That the parcels now have the entropy and temperature of the surrounding ambient plasma, but retain clumpy metallicity

distribution, suggests that turbulent mixing was not efficient here and that the gas was instead heated by conduction. The presence and shape of the isothermal front indicate that the magnetic field geometry in this region may be predominantly azimuthal. Furthermore, the absence of efficient turbulence indicates that HBI may operate unhindered in this region and that the instability may be more robust than suggested by some recent theoretical works (Ruszkowski & Oh 2010; Parrish et al. 2010). However, at least one more physical phenomenon may produce a similar magnetic field topology: Ruszkowski & Oh (2010) find that weak turbulent motions lead to trapped g-modes and result in gas motions that are preferentially tangential. They suggest that magnetic fields in clusters experiencing such g-modes can in principle become tangential even in the absence of thermal conduction and the HBI. While some thermal conduction seems to be implied in the case of the Virgo cluster, the concurrent presence of g-modes cannot be eliminated.

Juett et al. (2010) draw attention to what may be more circumstantial evidence for MHD instabilities. As much as 20% of the sample of 70 clusters presented by Snowden et al. (2008) have puzzling temperature profiles that appear to be quasi-isothermal at ∼Mpc radii.[10] The clusters show no signs of interaction, which could possibly have accounted for their temperature distribution, and they appear dynamically relaxed. Moreover, it is unclear whether models based on theoretical studies of cluster properties could account for this unusual class of objects (Nagai et al. 2007). If the class is shown to be unexpected, it may point to some missing physics in cosmological simulations. A possible explanation for the temperature structure of these objects is that thermal conduction operates very efficiently in their outer regions, an effect that arises as a natural consequence of the MTI instability. Radial configuration of magnetic field lines in outer regions of such clusters could only persist if they are isolated and unperturbed for sufficiently long periods of time, consistent with the observed properties of the quasi-isothermal clusters. Another line of evidence comes from the study of magnetic field structure around galaxies in the Virgo cluster. Pfrommer & Dursi (2010) find that in Virgo, which seems to be in transition to a cool core, the global magnetic field has a predominantly radial orientation at large radii, which again suggests the operation of MTI in its ICM.

In this study, we have evaluated the effects of two different physical mechanisms on the Faraday RM of a magnetized cooling-core cluster, in the context of the planned capabilities of the EVLA and SKA radio observatories. We compare a theoretical scenario in which conduction-driven MHD instabilities dominate the dynamics of the ICM, to a scenario in which magnetic field topology is defined by turbulent motions. We employ the polar shapelets image analysis method to efficiently detect patterns in the RM image with specific rotational symmetries, and thus classify their morphologies. Within the bounds of our simple models we find that the two mechanisms can produce strikingly different RM patterns and that future spectropolarimetric measurements will have sufficient sensitivity to discriminate between them that can be achieved in longer exposures with EVLA and relatively short exposures with SKA. We propose that the effect of the HBI and MTI instabilities be sought for in dynamically relaxed cooling-core clusters, and especially in the subclass of clusters with quasi-isothermal temperature profiles at large radii. More generally, it should be possible to discern physical mechanisms that result in qualitatively different magnetic field topologies from observed Faraday RM maps, without a priori knowledge about the nature of the processes. Such observations will enable detailed investigations into the behavior of MHD instabilities and other associated physical phenomena, which are of far reaching importance to a number of fundamental questions related to energy transport in clusters.

[10] The classification of the sample of quasi-isothermal clusters according to the thermal state of their cores has not been reported thus far.

We thank the anonymous referee for thoughtful comments which helped to significantly improve this manuscript. T.B. thanks Tracy Clarke and Richard Mushotzky for stimulating discussions and useful suggestions. Support for T.B. was provided by the National Aeronautics and Space Administration through Einstein Postdoctoral Fellowship Award Number PF9-00061 issued by the *Chandra* X-ray Observatory Center, which is operated by the Smithsonian Astrophysical Observatory for and on behalf of the National Aeronautics and Space Administration under contract NAS8-03060. T.B. and C.S.R. acknowledge support from the NSF under grant AST-0908212. R.M. is supported by STFC Advanced Fellowship PP/E006450/1 and FP7 grant MIRG-CT-208994.

REFERENCES

Balbus, S. A. 2000, ApJ, 534, 420
Balbus, S. A., & Reynolds, C. S. 2010, ApJ, 720, L97
Bogdanović, T., Reynolds, C. S., Balbus, S. A., & Parrish, I. J. 2009, ApJ, 704, 211
Bonafede, A., Feretti, L., Murgia, M., Govoni, F., Giovannini, G., Dallacasa, D., Dolag, K., & Taylor, G. B. 2010, A&A, 513, A30
Brentjens, M. A. 2011, A&A, 526, A9
Brentjens, M. A., & de Bruyn, A. G. 2005, A&A, 441, 1217
Carilli, C. L., & Rawlings, S. 2004, New Astron. Rev., 48, 979
Carilli, C. L., & Taylor, G. B. 2002, ARA&A, 40, 319
Churazov, E., Forman, W., Jones, C., & Böhringer, H. 2003, ApJ, 590, 225
Dewdney, P. E., Hall, P. J., Schilizzi, R. T., & Lazio, T. J. L. W. 2009, Proc. IEEE, 97, 1482
Enßlin, T. A., & Vogt, C. 2003, A&A, 412, 373
Feretti, L., & Giovannini, G. 2008, in A Pan-Chromatic View of Clusters of Galaxies and the Large-Scale Structure, ed. M. Plionis, O. López-Cruz, & D. Hughes (Lecture Notes in Physics, Vol. 740; Dordrecht: Springer), 143
Govoni, F., & Feretti, L. 2004, Int. J. Mod. Phys. D, 13, 1549
Guidetti, D., Murgia, M., Govoni, F., Parma, P., Gregorini, L., de Ruiter, H. R., Cameron, R. A., & Fanti, R. 2008, A&A, 483, 699
Jarvis, M. J., & Rawlings, S. 2004, New Astron. Rev., 48, 1173
Juett, A. M., Davis, D. S., & Mushotzky, R. 2010, ApJ, 709, L103
Kelly, B., & McKay, T. 2005, AJ, 129, 1287
Krause, M., Alexander, P., Bolton, R., Geisbüsch, J., Green, D. A., & Riley, J. 2009, MNRAS, 400, 646
Kuijken, K. 2008, A&A, 482, 1053
Laing, R. A., Bridle, A. H., Parma, P., & Murgia, M. 2008, MNRAS, 391, 521
Massey, R., & Refregier, A. 2005, MNRAS, 363, 197
Massey, R., Rowe, B., Refregier, A., Bacon, D. J., & Berg'e, J. 2007, MNRAS, 380, 229
Million, E. T., Werner, N., Simionescu, A., Allen, S. W., Nulsen, P. E. J., Fabian, A. C., Böhringer, H., & Sanders, J. S. 2010, MNRAS, 407, 2046
Murgia, M., Govoni, F., Feretti, L., Giovannini, G., Dallacasa, D., Fanti, R., Taylor, G. B., & Dolag, K. 2004, A&A, 424, 429
Nagai, D., Vikhlinin, A., & Kravtsov, A. V. 2007, ApJ, 655, 98
Padovani, P. 2011, MNRAS, 411, 1547
Parrish, I. J., & Quataert, E. 2008, ApJ, 677, L9
Parrish, I. J., Quataert, E., & Sharma, P. 2009, ApJ, 703, 96
Parrish, I. J., Quataert, E., & Sharma, P. 2010, ApJ, 712, L194
Parrish, I. J., & Stone, J. M. 2005, ApJ, 633, 334
Parrish, I. J., & Stone, J. M. 2007, ApJ, 664, 135
Parrish, I. J., Stone, J. M., & Lemaster, N. 2008, ApJ, 688, 905
Pfrommer, C., & Dursi, J. L. 2010, Nat. Phys., 6, 520
Quataert, E. 2008, ApJ, 673, 758
Roettiger, K., Stone, J. M., & Burns, J. O. 1999, ApJ, 518, 594
Ruszkowski, M., & Oh, S. P. 2010, ApJ, 713, 1332

Schilizzi, R. T., et al. 2007, SKA Memo 100, http://www.skatelescope.org
Simard-Normandin, M., Kronberg, P. P., & Button, S. 1981, ApJS, 45, 97
Snowden, S. L., Mushotzky, R. F., Kuntz, K. D., & Davis, D. S. 2008, A&A, 478, 615
Stepanov, R., Arshakian, T. G., Beck, R., Frick, P., & Krause, M. 2008, A&A, 480, 45
Strauss, M. A., Huchra, J. P., Davis, M., Yahil, A., Fisher, K. B., & Tonry, J. 1992, ApJS, 83, 29
Taylor, A. R. 2008, in IAU Symp. 248, A Giant Step: from Milli- to Micro-arcsecond Astrometry, ed. W. J. Jin, I. Platais, & M. A. C. Perryman (Cambridge: Cambridge Univ. Press), 164
Victor, J. D., Mechler, F., Ohiorhenuan, I., Schmid, A., & Purpura, K. P. 2009, J. Neurophysiol., 102, 3414
Wilman, R. J., et al. 2008, MNRAS, 388, 1335
Young, C. A., Gallagher, P. T., Ireland, J., & McAteer, R. 2005, Am. Geophys. Union Spring Meeting Abstracts, A7